Linking total precipitable water to precipitation extremes globally

Seokhyeon Kim[1], Ashish Sharma[1], Conrad Wasko[2], and Rory Nathan[2]

[1]School of Civil and Environmental Engineering, University of New South Wales, Sydney, NSW 2052, Australia

[2]Department of Infrastructure Engineering, The University of Melbourne, Vic 3010 Australia

Corresponding author: Seokhyeon Kim (seokhyeon.kim@unsw.edu.au)

Key Points:

- The relationship between daily extreme precipitation (EP) and total precipitable water (W) is investigated at the global scale.
- W exhibits statistically significant upward trends that are predominant worldwide, especially in tropical regions.
- The W-EP relationship is most pronounced over the tropics (within ±30°) and is noticeably reduced elsewhere.

This article has been accepted for publication and undergone full peer review but has not been through the copyediting, typesetting, pagination and proofreading process, which may lead to differences between this version and the Version of Record. Please cite this article as doi: 10.1029/2021EF002473.

Abstract

The relationship between extreme precipitation (EP) and precipitable water (W) is useful to assess design extremes and speculate on their expected changes with rising global temperatures. This study investigates the relationship between daily and longer duration EP and corresponding W at a global scale by analysing remote-sensed and reanalysis datasets from 2003–2019. An assessment of the consistency in the temporal trend across various W datasets reveals a consistent statistically significant upward trend during the period. This upward trend, while predominant worldwide, is especially significant over tropical land regions. W is found to generally be positively correlated with surface (dew point) temperature, suggesting a rise in temperature will cause a greater W over time. To assess whether EPs occur coincident with extreme W, the Concurrent Extremes Index (CEI) is proposed, which compares the cumulative distribution functions between the two variables and assumes a value of unity if ranks of the EP series are identical to that of the coincident W series, and zero with no correspondence. For EP (defined as the five largest 1-day events per year on average), a high CEI is pronounced across the tropics, except for rainforests. The W-EP relationship is noticeably weakened in non-tropics, except the inland regions of North America and East Asia. An assessment indicates that as the duration of the EP becomes longer, the influence of W on EP decreases. However, the contrast in the W-EP relationship between the tropics and non-tropics is found to become more pronounced as longer-duration EPs are considered.

Plain Language Summary

How a rise in temperature will affect extreme precipitation becomes an important question as we try and adapt existing infrastructure and build new infrastructure to withstand extreme events of the future. This study investigated the relationship between extreme precipitation (EP), atmospheric precipitable water (W), and temperature using 17 years of global daily data. We first examined the temporal trend of W as well as its correlation with temperature to identify changes that can be expected into the future. The results showed that, across the world, W consistently trends upwards and exhibits strong correlation with temperature, this being particularly so over tropical land areas. An investigation into the relationship between EP and coincident W suggests the relationship becomes stronger in the tropics, especially when daily durations are considered, suggesting the increase in W over time can be expected to lead to more intense extreme precipitation events of daily or shorter durations. Longer duration events and colder latitudes (outside of the tropics) exhibit a weaker relationship, suggesting the increase in W expected with time may have reduced impacts on non-tropical extreme precipitation events.

1. Introduction

Climate change has noticeably altered extreme precipitation (EP) events, impacting human life and endangering built infrastructure around the world (IPCC, 2021; Sih et al., 2011). Many studies report increase in EP globally or regionally for much of the last century (Alexander et al., 2006; M. G. Donat et al., 2013; Markus G. Donat et al., 2016; Sun et al., 2021), with EP projected to become more severe and frequent as temperatures rises with global warming (Bao et al., 2017; Prein et al., 2017; Sillmann et al., 2013; Westra et al., 2014). Increasing temperatures and EP also affect the estimation of design extremes such as intensity-frequency-duration relationships (Sharma et al., 2021) and rarer extremes including the probable maximum precipitation (PMP) (Kunkel et al., 2013). Existing infrastructure, with designs based on past EP patterns, do not appear to be effective any longer (Chester et al., 2020; Wright et al., 2019), especially when considering recent severe floods in countries around the world (Syvitski & Brakenridge, 2013; Worawiwat et al., 2021; World Bank, 2012). In particular, recent European floods in 2021 were the result of a large-scale storm event that first impacted the United Kingdom then advanced to several countries in central Europe, causing more than 200 casualties and more than 2.5 billion euros of property damage (BBC, 2021; Cornwall, 2021). China has also experienced severe country-wide flooding in 2020 and 2021, resulting in a tremendous toll on human life and property (Guo et al., 2020). In the face of such threatening realities, it is essential to understand future changes in EP due to climate change and reasonably reflect the changes in various policies and design codes (Wasko et al., 2021).

Future changes in EP are usually projected using General Circulation Models (GCMs). GCMs represent the physical processes in the global climate system, allowing simulation of the response to increasing greenhouse gas concentrations (i.e., increasing temperature). Many studies based on GCMs (often suitably downscaled to finer spatial resolutions) have noted that projected increases to EP in tropical regions are more severe than those in other regions, but with greater uncertainty. For example, using 18 climate model-derived simulations from the World Climate Research Program's (WCRP's) Coupled Model Intercomparison Project phase 3 (CMIP3) archive, Paul A. O'Gorman (2012) showed that the tropical sensitivity (%/K) of the 99.9th percentile of daily precipitation is double that of the extratropics. However, O'Gorman and Schneider (2009), assessing the 99.9th percentile of daily precipitation under moderate greenhouse conditions, showed simulations over the tropics are not consistent across climate models, recommending improvements in characterising upward velocities in the climate models for better EP predictions.

More recently, using CMIP5 simulations, Kharin et al. (2013) also showed greater EP sensitivities with temperature over the tropics than the subtropics. EP was projected to be more frequent, exhibiting a 6–20%/K sensitivity with global temperature in the tropics, but again with greater uncertainty than the sensitivities in the subtropics. Correspondingly, Kim et al. (2020) showed that daily EP projections from 45 CMIP5 model outputs consisting of various models, ensembles, and emission scenarios are highly uncertain over the tropics. In particular, the greatest variability in EP is observed across models rather than across ensembles or scenarios, and the relative uncertainty normalized by the regional precipitation amount is greatest in dry regions. Kunkel et al. (2013) found significant increases in average and maximum water vapor concentrations in the seven CMIP5 simulations, suggesting that rare precipitation extremes up to the PMP may increase in the future. Indeed, Prein et al. (2017) found that hourly EP increases with temperature in moist, energy-limited environments, but found sharp decreases in dry, moisture-limited environments. It has hence been suggested that the dynamic contribution to EP plays an

important role in reducing uncertainty in future projections of regional extremes (Pfahl et al., 2017).

An alternative to relying on GCMs for EP projection is to use the principle of rare event simulation where covariates such as surface air temperature (SAT), dew point temperature (DPT), or integrated water vapor (or total precipitable water, W) are projected and used to derive the EP instead of computational expensive alternatives involving direct samples of EPs (Roderick et al., 2020). The EP projections use sensitivities, correlations, or joint likelihoods between EPs and relevant causative variables (covariates) the relationship for which can be established using historical data. The temperature-variable sensitivity, usually expressed as %/K, is also called "scaling", often based on the Clausius-Clapeyron relation of 6–7%/K (i.e., CC scaling) for global-mean water vapor. Such a scaling approach to EP projection has been the basis of many studies at various timescales with increasing temperature and found to perform similar to climate model projections of EP (Geert Lenderink & Attema, 2015; Manola et al., 2018). An added factor that makes such studies attractive is the relatively high stability GCMs exhibit for the covariates typically used (SAT, W), when compared to directly sampled EP events (Eghdamirad et al., 2017; Johnson & Sharma, 2009; Kim et al., 2020).

Scaling studies generally use SAT to examine the relationship between EP and temperature. For example, Utsumi et al. (2011) analysed global in- situ daily precipitation and SAT and found that the EP increases at high latitudes but decreases in the tropics with increasing SAT, which is consistent with Wasko et al. (2016) who used remotely sensed precipitation and SAT. Ali and Mishra (2017) found that the negative scaling between EP and SAT in India becomes positive when DPT is used instead and suggesting DPT is more linked to EP than SAT (Barbero et al., 2018; G. Lenderink et al., 2011). Similarly, Wasko et al. (2018) found stronger associations of DPT with EP as compared to SAT using in-situ data across Australia. W. Zhang et al. (2019) also found strong negative scaling between daily EPs and SAT in the tropics, deducing the reason as limitations in moisture availability under the high-temperature bands, and regarded DPT as a better measure for estimating the EP sensitivity. Indeed, a global study using DPT as a scaling covariate found more positive scaling when DPT was used as opposed to SAT, with even more positive scaling once temperature seasonality is accounted for Ali et al. (2018). However, recent studies suggest that the negative scaling in the tropics may be due to a limited consideration for sub-daily temperature variations resulting from precipitation, with positive scaling obtained over the tropics when sub-daily SAT prior to storm events is used as a covariate (Visser et al., 2020).

Although less studied, probably due to limited observations in space and time, a promising covariate for projecting EP is the integrated water vapor or total precipitable water (W). Here, W is generally defined as the column of integrated water vapor from land surface elevation to the top of the troposphere. Using W for EP projections is advantageous for the following reasons. First, W exhibits a distinct dependence on temperature in general, making it an important attribute of climate change (Fujita & Sato, 2017; Ho et al., 2018; Kunkel, Karl, et al., 2020; Mears et al., 2007; Mears et al., 2018; Nayak & Takemi, 2019; P. A. O'Gorman & Muller, 2010; Roman et al., 2015). Second, unlike precipitation estimation, W estimated using satellites and models (i.e., reanalyses) agrees well with radiosonde-based observations (Bock et al., 2005; Jiang et al., 2019; X. Li & Long, 2020; Shi et al., 2018; Y. Wang et al., 2017). Finally, and most importantly, W has been regarded as a potential predictor for EP in both data and model outputs due to its stronger correlation with rainfall than SAT or DPT alone (Roderick et al., 2020).

2. Background

Atmospheric mass balance (Su & Smith, 2021) can be expressed as the temporal change of total precipitable water:

$$\frac{\partial W}{\partial t} = E - P - \nabla \cdot Q \quad (1)$$

where, W: total precipitable water; t: time; E: evaporation; P: precipitation; Q: water vapor convergence computed as the convergence of zonal and meridional water vapor transport vector, i.e., $Q = (Q_x, Q_y)$; and $\nabla \cdot Q$ is the combined magnitude of Q.

Given extreme precipitation typically dominates the other flux terms in (1), many attempts have been made to link W to rare to probable maximum precipitation (PMP) events as the basis for risk assessment for existing and new infrastructure. The PMP is defined as "the greatest accumulation of precipitation for a given duration meteorologically possible for a design watershed or a given storm area at a particular location at a particular time of year" (WMO, 2009). In estimating the PMP the historically observed EP is maximized based on the ratio of the historically observed maximum W and the W corresponding to the historical EP (Kunkel et al., 2013). In other words, a linear relationship is assumed between EP and W, with the PMP ascertained as the EP that could occur were W at its historical maximum. Change in W as a result of global warming hence has direct implications on the estimated PMP. Based on this premise, Kunkel et al. (2013) assessed several CMIP5 GCM simulations under the most severe greenhouse gas emission scenarios and projected that W will increase by at least 20% globally in the 21st century, and concluded that the PMP will similarly increase.

While several continental-scale studies agree that W increases with increasing temperature (or climate change) (Bao et al., 2017; Kunkel, Stevens, et al., 2020; Roderick et al., 2019; D. Zhang et al., 2013), there are various arguments as to whether an increase in W leads to an increase in EP over the different continental regions. For example, D. Zhang et al. (2013) found a significant upward trend in W especially in summer over the Tibetan Plateau, but no significant increase in precipitation. Using gauge rainfall observations and remotely sensed integrated water vapor (i.e., W) Roderick et al. (2019) found a strong positive correlation between W and EP across Australia, including the tropical regions in the north. However, Bao et al. (2017), using a regional climate model simulations across Australia, found that although daily EP (99th percentile) projections are highly correlated to W, they increase at a greater rate than could be attributed to the increase in W alone. Kunkel, Karl, et al. (2020) suggested that increasing W contributes to increases in EP across the contiguous United States, based on observing statistically significant upward trends of EP that are concurrent with those of W. Indeed Kunkel, Stevens, et al. (2020) also found positive correlations between W and EP at over a third of over 3,000 observatories in the United States, and found that, in general, EP is linearly proportional to W, but non-linear at both extremes of the W distribution. Hence, they concluded that W is the key limiting factor in the most intense EPs.

However, a global picture of the relationship between W and EP does not exist. Moreover, with the advent of many new remote sensed W observations, there is no comprehensive evaluation of the W-EP relationship between the alternate data products that have been developed to characterise W. Using 17-years of data from 2003 to 2019, this study aims to provide a comprehensive evaluation of the W-EP relation building on the continent-scale studies presented above (Bao et al., 2017; Kunkel, Karl, et al., 2020; Kunkel, Stevens, et al., 2020; Roderick et al.,

2019, 2020). Using a simple but consistent approach at a global scale we answer three primary questions:

1. How is W impacted by climate change?
2. Does EP correspond to coincident W extremes, and whether this correspondence is homogenous in space?
3. Does this correspondence hold across different durations and thresholds of EP?

To answer Q1, we prove the relevance to climate change by identifying the temporal trend of W along with its correlation with temperature, and show that the results are robust by using various remotely sensed and reanalysis W data (Section 4.1). Second, to answer Q2 and Q3, we investigate the W-EP relation using spatially distributed correspondence metrics and assess sensitivity across different rainfall durations and depth thresholds (Section 4.2). Lastly, we discuss the implications of our results in the context of climate change projections, outlining the impacts that can be expected to unfold to EP into the future.

3. Data and Methods

3.1. Data

This study analyses the relationship between extreme precipitation (EP) and concurrent total precipitable water (W) at a global scale with respect to coincident surface air (SAT) and dew point (DPT) temperature information. For precipitation, we use the Integrated Multi-satellite Retrievals for the Global Precipitation Measurement (GPM IMERG) final product (Huffman et al., 2015). While we select the GPM IMERG final product which shows superior performance compared to other products (Beck et al., 2019) without shortening the study period, the results need to be considered in context of the performance and uncertainty of the data presented in existing evaluation studies (O et al., 2017; Yu et al., 2021). For precipitable water, we focus on the Atmospheric Infrared Sounder (AIRS) (AIRS project, 2019), utilizing four additional reanalyses datasets to check consistency in the results, these being the second Modern-Era Retrospective Analysis for Research and Applications (MERRA2) (Gelaro et al., 2017); European Centre for Medium-Range Weather Forecasts (ECMWF) reanalysis version 5 (ERA5) (Hersbach et al., 2020); the Japanese 55-year Reanalysis (JRA-55) Kobayashi et al. (2015); and the National Centers for Environmental Prediction (NCEP) (Saha et al., 2010; Saha et al., 2014). The study period is 17 years from January 1, 2003, to December 31, 2019, which ensures concurrency with the period of AIRS, which is the shortest dataset used. Along with these, we use the 2-m surface air temperature (SAT) and the 2-m dew point temperature (DPT) from ERA5-Land to investigate how P and W are related to both. The details of the datasets are summarized in Table 1.

Table 1. Summary of datasets used in this study

Data		Variable name	Spatial resolution	Temporal resolution
Total precipitable water (mm)	AIRS (V7.0, AIRS-only)	Retrieved Total Precipitable H2O Vapor	1°	Daily (ascending /descending)
	MERRA2 (V5.12.4, M2T1NXINT)	Total precipitable water vapor (TQV)	0.5° × 0.625°	Hourly

	ERA5 (on single levels)	Total column water vapour	0.25°	Hourly
	JRA-55 V6.6.2	Total Precipitable Water	1.25°	6-hourly
	NCEP V1/V2	Total Precipitable Water	0.312°	6-hourly
Precipitation (mm)	GPM-IMERG Final V6	Daily accumulated precipitation	0.10°	Daily
Temperature (K)	ERA5-Land SAT/ DPT	2 metre temperature /2 metre dewpoint temperature	0.25°	Hourly

The following processing has been applied for the datasets. First, all data used for this study are temporally averaged to a daily time step. For AIRS, data gaps between satellite scanning swaths are simultaneously filled by the three-dimensional discrete cosine transforms (DCT-PLS) to minimise data loss (Garcia, 2010; Pham et al., 2019; G. Wang et al., 2012). Next, for the trend analysis, we use monthly W data which are computed from the daily, unless monthly data was originally provided from the data sources. Lastly, the data products are resampled onto a spatial resolution of 1° (approximately 100 km at the equator) using spatial-averaging resampling.

3.2. Methods

From the mass balance (1), we focus on W and P and examine the relationship between temperature (T) and W and P to evaluate the expected changes associated with rising temperatures. In this context, we first investigate the temporal trend of W and its correlation with temperature (Section 3.2.1). After that, we measure the correspondence of W with P, especially EP (Section 3.2.2), using the methods described below.

3.2.1. Trend of W and W-T relationship

To see if the monthly W data have increasing or decreasing trends over the study period, we utilize the Mann-Kendall (MK) test (Hirsch et al., 1982; Kendall, 1948; Mann, 1945). The MK test rejects the null hypothesis (H_0) or accepts the alternative one (H_1) based on a two-sided test. Here, H_0: a data sample ($x_1 \ldots x_n$) consists of independent and identically distributed (IID) random variables; H_1: x_i and x_j are not IID for all i, j ($i \neq j$). For this, the test statistic S is defined as

$$S = \sum_{i=1}^{n-1} \sum_{j=i+1}^{n} \mathrm{sgn}(x_j - x_i) \quad (2)$$

where,

$$sgn(\theta) = \begin{cases} 1 & \text{if } \theta > 0 \\ 0 & \text{if } \theta = 0 \\ -1 & \text{if } \theta < 0 \end{cases}$$

Considering the seasonality in W (Jiang et al., 2019), we adopt the Seasonal Kendall (SK) test (Helsel & Hirsch, 1992) using the Theil-Sen slopes (Sen, 1968; Theil, 1992). When the number of data points n >20, the upper (U) and lower (L) confidence limits for the Theil–Sen slopes are given as (3), respectively (Helsel & Hirsch, 1992).

$$\mathrm{U} = \frac{N + Z_{\alpha/2}\sqrt{\frac{n(n-1)(2n+5)}{18}}}{2} + 1$$
$$\mathrm{L} = \frac{N - Z_{\alpha/2}\sqrt{\frac{n(n-1)(2n+5)}{18}}}{2} \quad (3)$$

where, $N = n(n-1)/2$ (number of pairwise slopes); $Z_{\alpha/2}$: critical value having a p-value corresponding to the half of a significance level α (i.e., $\alpha/2$), obtainable from a standard normal distribution table.

In the SK test, the overall statistic S_k reflecting the seasonality is calculated as

$$\mathrm{S}_k = \sum_{s=1}^{\mathrm{m}} \mathrm{S}_s \quad (4)$$

where, S_s is the Kendall's S statistic for each season (s=1, …, m). In this study, each month in the study period is regarded as each season (i.e., m=12).

When the product of the total number of seasons and the number of years in the study period exceeds 25, the distribution of S_k approaches a Normal distribution (Hirsch et al., 1982). Then the standard normal deviate $\mathrm{Z}_{\mathrm{S}_k}$ is estimated as (5), and is evaluated accordingly. Here, the expected value of S_k equals 0 and the standard deviation is σ_{S_k}. In the two-sided SK test, given the critical value Z_c at a probability of exceedance of $\alpha/2$, H_0 is rejected when $|\mathrm{Z}_{\mathrm{S}_k}| > \mathrm{Z}_c$, for which we consistently use α=0.05 in this study.

$$\mathrm{Z}_{\mathrm{S}_k} = \begin{cases} \dfrac{\mathrm{S}_k - 1}{\sigma_{\mathrm{S}_k}} & \text{if } \mathrm{S}_k > 0 \\ 0 & \text{if } \mathrm{S}_k = 0 \\ \dfrac{\mathrm{S}_k + 1}{\sigma_{\mathrm{S}_k}} & \text{if } \mathrm{S}_k < 0 \end{cases} \quad (5)$$

where,

$$\sigma_{\mathrm{S}_k}{}^2 = \sum_{i=1}^{\mathrm{m}} \frac{\mathrm{n}_s(\mathrm{n}_s - 1)(2\mathrm{n}_s + 5)}{18}$$

n_s=number of data in season s

3.2.2. Data Concurrence Index

Once the Theil-Sen slopes are estimated for each monthly W dataset, the concurrency in the results are evaluated based on the Data Concurrence Index (DCI) (Anabalón & Sharma, 2017; Kim et al., 2021) defined as:

$$\mathrm{DCI} = \frac{1}{\mathrm{N}} \sum_{i=1}^{\mathrm{N}} \frac{\mathrm{h}_i \mathrm{T}_i}{|\mathrm{T}_i|} \tag{6}$$

where, N: number of datasets used for the trend analysis (i.e., N=5); T_i: trend magnitude; h_i: 1 for significant trend at a significance level (α=0.05) otherwise 0 for ith dataset. That is, the closer a DCI is to 1 (-1), the more concurrently the datasets show significant upward (downward) trends. On the other hand, a DCI close to zero means that the trends are not statistically significant or are inconsistent across the datasets.

3.2.3. Concurrent Extremes Index (CEI)

In this study, we define EPs as the five largest 1-day events per year on average. To sample these events, we use the 85th largest value (17 years × five 1-day events) as the threshold for all daily precipitation values in each grid cell. By applying the threshold for each year, five 1-day events are selected in each year on average. A minimum interval of 4 days between two events is applied to help ensure that the events selected are independent. For the sensitivity analysis, we also consider samples based on 5-day event intervals and/or 10 events per year.

The W-P relation is first investigated by the Pearson correlation (R) between overall P (or EP) and concurrent W. In contrast to the W-T relationship (presented in Section 4) we find that the W-EP relationship differs regionally. That is, in some regions EP increases with W, but not in others. A measure of similarity between EPs and coincident W is proposed. This measure, termed the Concurrent Extremes Index (CEI), can be expressed as:

$$\mathrm{CEI} = 1 - \frac{E[F_P(EP) - F_W(W|EP)]}{E[F_P(EP) - 0.5]} \tag{7}$$

where $F_X(\cdot)$ denotes the Cumulative Distribution Function (CDF) for variable X and $E(\cdot)$ represents the expectation operator. The CEI assesses the expected difference in the Cumulative Distribution Function (CDF) of EP and coincident W, under the premise that if the EPs occur coincident with extreme W, CEI will be unity, while if there is no relation between the two variables ($F_W(W|EP)$ = 0.5), it will equal zero.

While metrics such as rank correlation have the advantage of being less sensitive to outliers, their direct use here is not possible as they use the complete rank distribution of the data. The CEI, on the other hand, focusses just on the extreme events, while still having the intuitiveness of a measure such as the correlation, as it is defined to scale from 0 to 1.

3.2.4. Result interpretation

In order to summarise the analysis results, we use the 33 regions used for the Intergovernmental Panel on Climate Change (IPCC)'s Fifth Assessment Report (AR5) (Seneviratne et al., 2012). Here, the 33 AR5 regions are composed of 26 Special Report on Climate Extremes (SREX) regions and 7 non-SREX ones. For readers here, the original short names of the 33 regions are presented in the caption of Figure 1, and the full names and spatial boundaries can be found at https://www.ipcc-data.org/guidelines/pages/ar5_regions.html.

For simplicity, the W-EP relationship calculated using the CEI (eq. (7)) is clustered into several regions (Figure 4b) by using an adaptive K-means clustering algorithm (Dixit, 2021). The adaptive K-means clustering algorithm does not need to specify the number of clusters. Instead, the cluster centroid is found sequentially, starting with the mean of all data points as the initial cluster centroid, iteratively excluding data points whose Euclidean distance to the cluster centroid is greater than the mean distance, and updating the cluster centroid with the mean of the remaining data points.

4. Results

We first present the W trend and the W-T relationship (Section 4.1), followed by the W-P relationship in Section 4.2. The results presented are based on the AIRS dataset that has been widely used in previous studies and showed good performance compared to reanalyses and radiosonde observations (Jiang et al., 2019; Roderick et al., 2019, 2020; Y. Wang et al., 2017). The other W datasets have been limited to evaluating concurrency in the results based on the DCI and other measures. Hence, unless otherwise indicated, the W here is from AIRS.

4.1. W trends and W-T relations

We begin by analysing the monthly global mean W time series to assess trends among the datasets in Table 1 and present the results in Table 2. All data for 17 years from 2003 to 2019 show an average value of about 24 mm/month and present statistically significant upward trends, although NCEP shows a considerably smaller trend magnitude compared to the other datasets.

Table 2. Global W mean and trend over 17 years from January 2003 to December 2019, estimated using global monthly W time series from five W datasets.

Dataset	Monthly Mean (mm/month)	Trend (Sen's slope) (mm/month/year)	Confidence Interval (95%, lower/upper)		Significant (α=0.05)
AIRS	25.3	0.0435	0.0367	0.0498	Yes
MERRA2	24.5	0.0485	0.0412	0.0557	Yes
ERA5	24.3	0.0471	0.0417	0.0532	Yes
JRA-55	25.3	0.0412	0.0340	0.0484	Yes
NCEP	24.7	0.0100	0.0035	0.0168	Yes
Mean	24.8	0.0369	0.0310	0.0432	Yes

Although there appears to be a consistency globally between the data sets, it may be expected that the trend will vary spatially. Figure 1 presents global maps of the monthly W trend (Figure 1a) and the DCI for the W trends estimated from the five monthly W datasets including AIRS (Figure 1b) on a grid cell basis. Figure 1c presents boxplots of monthly W trend magnitudes (mm/month/year) for the 33 IPCC AR5 regions. The Pearson correlation (R) between daily W and concurrent SAT (Figure 2a) and DPT (Figure 2b) are also presented.

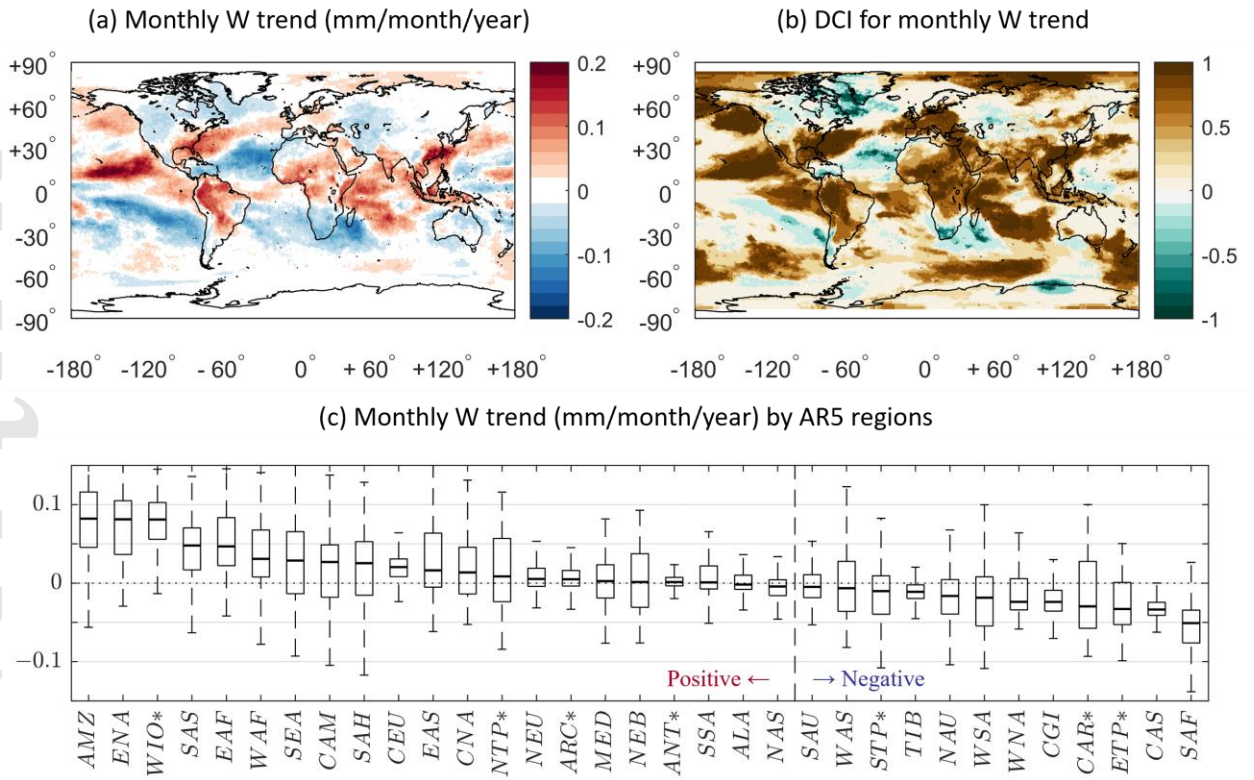

Figure 1. Results of monthly W trend analysis across 17 years from 2003 to 2019. (a) monthly W trend; (b) DCI for monthly W trends using five monthly W datasets; (c) Monthly W trend magnitudes (mm/month/year) in descending order for the 33 IPCC AR5 regions, consisting of 26 SREX and 7 non-SREX regions (marked by asterisks). Here, AMZ: Amazon; ENA: East North America; WIO*: West Indian Ocean; SAS: South Asia; EAF: East Africa; WAF: West Africa; SEA: Southeast Asia; CAM: Central America/Mexico; SAH: Sahara; CEU: Central Europe; EAS: East Asia; CNA: Central North America; NTP*: Pacific Islands region; NEU: North Europe; ARC*: Arctic; MED: South Europe/Mediterranean; NEB: North-East Brazil; ANT*: Antarctica; SSA: Southeastern South America; ALA: Alaska/N.W. Canada; NAS: North Asia; SAU: South Australia/New Zealand; WAS: West Asia; STP*: Southern Topical Pacific; TIB: Tibetan Plateau; NAU: North Australia; WSA: West Coast South America; WNA: West North America; CGI: Canada/Greenland/Iceland; CAR*: small islands regions Caribbean; ETP*: Pacific Islands region; CAS: Central Asia; SAF: Southern Africa.

As depicted in Figure 1a, upward trends are dominant over most tropical land surfaces (±30°) including the Florida coastline in the United States, most of the Amazon, Central Africa, India, Southeast Asia Archipelago, and Southeast China. The magnitude of the upward trends tends to decrease away from the tropics. On the other hand, downward (or weakly upward) trends are observed in North America including Greenland, Northern Europe, Central and East Asia, the south end of South America, and southern Africa, and central and northern Australia. The trends of W over the ocean are mixed, and downward trends are notable in some regions of the South Pacific, North Atlantic, and South Indian Oceans. Segmenting the trend magnitudes by the 33 IPCC AR5 regions (Seneviratne et al., 2012), the results are presented as boxplots in Figure 1c. Regions with positive means are a total of 21 on the left, from AMZ (Amazon) to Southeast South America (SSA), and regions with negative means are a total of 12 on the right, from SAU (South

Australia/New Zealand) to SAF (South Africa). Among them, except for the seven non-SREX regions marked by asterisks in the boxplot, the three regions showing the largest upward trends are AMZ (Amazon), ENA (East North America), and SAS (South Asia). On the contrary, the three regions showing the greatest downward trends are SAF (Southern Africa), CAS (Central Asia), and CGI (Canada/Greenland/Iceland).

The spatial pattern of the trends in Figure 1a matches that of DCI in Figure 1b with a strong correspondence between data sets over land in the tropics as well as over Europe. Here, regions where two or more of the five datasets show upward trends account for 44% of the world (i.e., DCI $\geq$ 0.4), whereas only 3% of the regions have two or more datasets that show downward trends (i.e., DCI $\leq$ -0.4). Moreover, the difference between the areas exhibiting upward and downward trends becomes larger when further considering a DCI of ±0.2: 58% (upward trend) and 11% (downward trend). In summary, during the 17-year study period, the dominant worldwide trend in monthly W is upward, and this is more pronounced in the tropical regions within ±30°, especially over the land.

The spatial distribution of the Pearson correlation (R) between daily W and both SAT and DPT is shown in Figure 2.

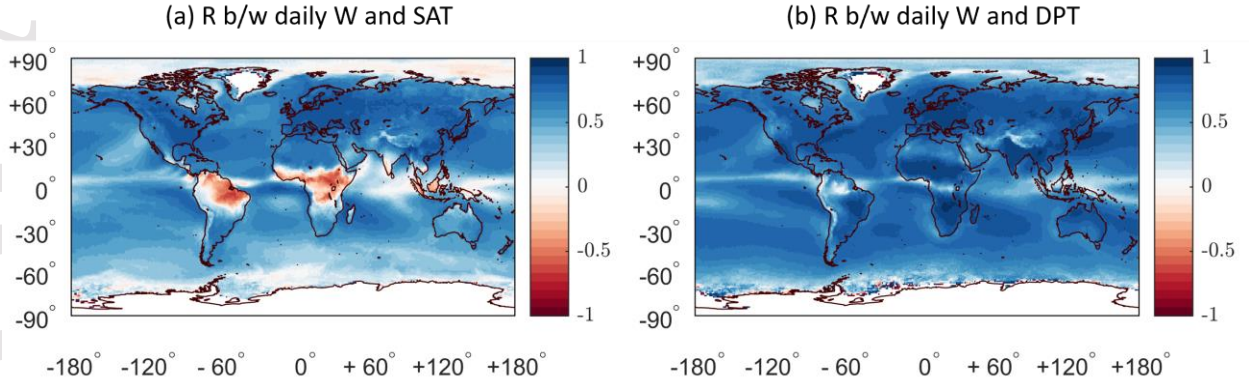

Figure 2. Pearson correlation (R) between daily W and temperature across 17 years from 2003 to 2019. (a) R between daily W and SAT; (b) R between daily W and DPT.

As shown in Figure 2a, most regions show positive R, while weak to moderate negative R is observed over land in the Amazon, central Africa, and southeast Asia. Roderick et al. (2019) found that increases in SAT (> 28°C) are not proportional to increases in integrated water vapor in the tropics of northern Australia, which can be explained by interactions between surface temperature and surface moisture in hot climates. Namely, when a lack of surface moisture leads to a high SAT, the conversion of additional radiation into sensible, instead of latent, heat is likely to occur. As a result of this chain, high SAT tends to be accompanied by low integrated water vapor. Alternatively, as the regions where negative R is observed are strongly associated with the global rainforests such as the Amazon, Congo, and the Southeast Asian Archipelago (Encyclopedia Britannica, 2020). Such negative correlations may be partially attributed to local cooling due to evapotranspiration (Ellison et al., 2017; Lejeune et al., 2015; Y. Li et al., 2015) or precipitation (Bao et al., 2017; Visser et al., 2020). Unlike the case with SAT, the relationship between W and DPT shows strong positive R almost universally globally (Figure 2b). These results suggest that W is generally positively correlated with SAT and/or DPT across the globe, suggesting that rising temperature with climate change may be leading to increases in W.

4.2. W-P relationship

As mentioned earlier, EP in this study is defined as the five largest 1-day events per year on average (hereafter simply referred to as '1D5E'). We begin examining the W-P relationship by presenting the R between overall P and W (Figure 3a), and the R between EP and corresponding W (Figure 3b). Hereafter, the former is referred to as R_{OV}, and the latter, R_{EP}, for brevity. We restrict our analysis data pairs where SAT > 273.15 K and P > 1 mm to remove snow events. In addition, we exclude high-latitude regions (outside ±60°) where many data gaps exist due to snow/ice surfaces (Huffman et al., 2015). Scatterplots over two regions, northern Germany in Figure 3c and northern Australia in Figure 3d, where the W-P relationship differs greatly are also presented.

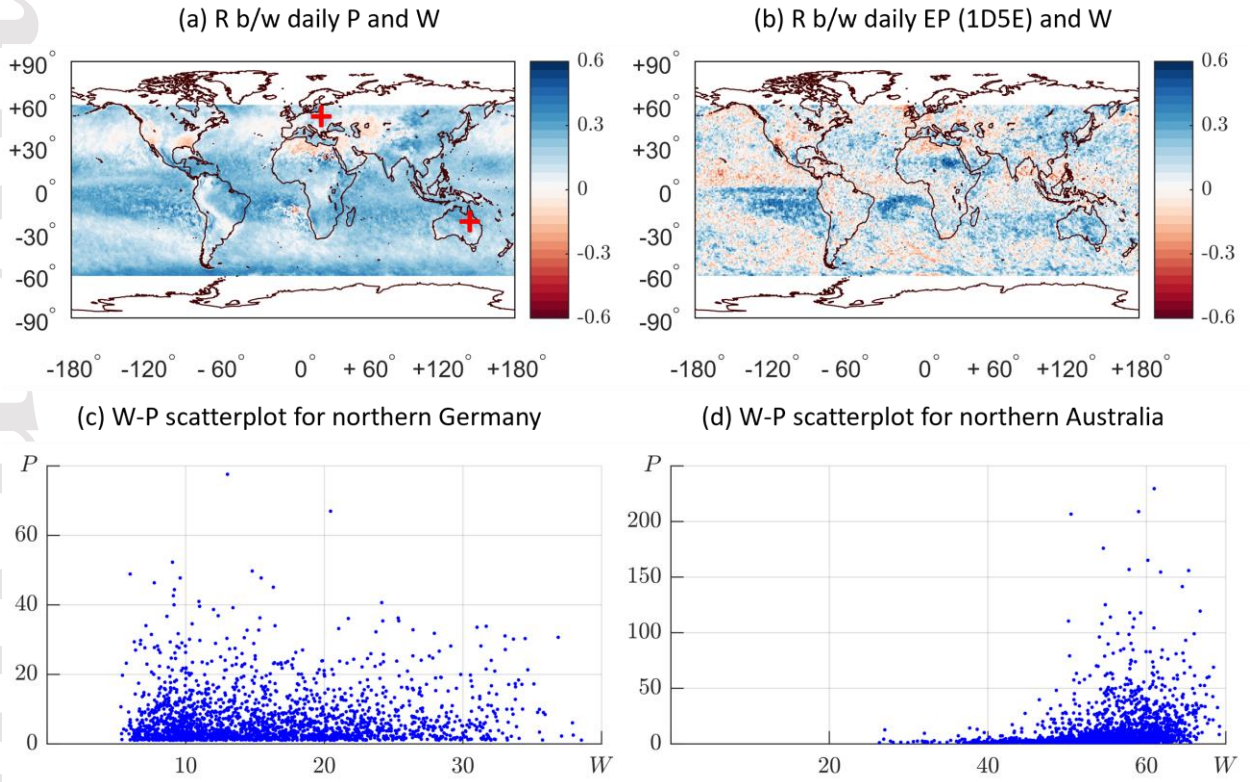

Figure 3. W-P relationship, presenting (a) R between overall P and W (i.e., R_{OV}); (b) R between EP (1D5E) and corresponding W (i.e., R_{EP}); (c) and (d) W-P scatterplots for two locations, northern Germany, and northern Australia, respectively, marked as red crosses on (a). Here, the units for both W and P is 'mm/day'.

In contrast to the clear W-T relationship represented by the moderate to strong R between W and SAT(DTP) presented in Figure 2a and b, R_{OV} in Figure 3a shows overall weak to moderate positive magnitudes. Weak negative correlations are also observed in some regions including the eastern and western coastal areas of North America, North Africa, the northern part of the Arabian Peninsula, and the inland regions of Central Asia. Even if the correlation is constrained to considering only EP as shown in Figure 3b, the W-P relationship does not appear to be consistent spatially. R_{EP} in Figure 3b exhibits moderately positive values in some regions including parts of North Africa and Australia, but in many regions, the EP and W do not appear to be correlated.

The scatter plots shown in Figure 3 (c, d) suggest that there is a weak relationship between P and W, though this portrayal of correlation ignores the conditional nature of the dependence involved. In northern Germany (Figure 3c), the W values corresponding to the EPs are widely scattered suggesting that a large P can occur with any value of W, whereas in northern Australia (Figure 3d), the W values for the EPs tend to be concentrated over a narrow range of high values. That is, in determining the strength of the relationship between W and P it is important to quantify the conditional dependence of W on EP, not the simple linear correlation between the two variables. Taking this into account, , we calculate the Concurrent Extremes Index (CEI) corresponding to EPs. For example, for northern Germany belonging to CEU (Central Europe) the median CEI is 0.63 representing less relevance of W to EP. Alternatively, for northern Australia, part of NAU (North Australia), the median CEI is 0.87 indicating a strong relevance of W to EP (Figure 4c).

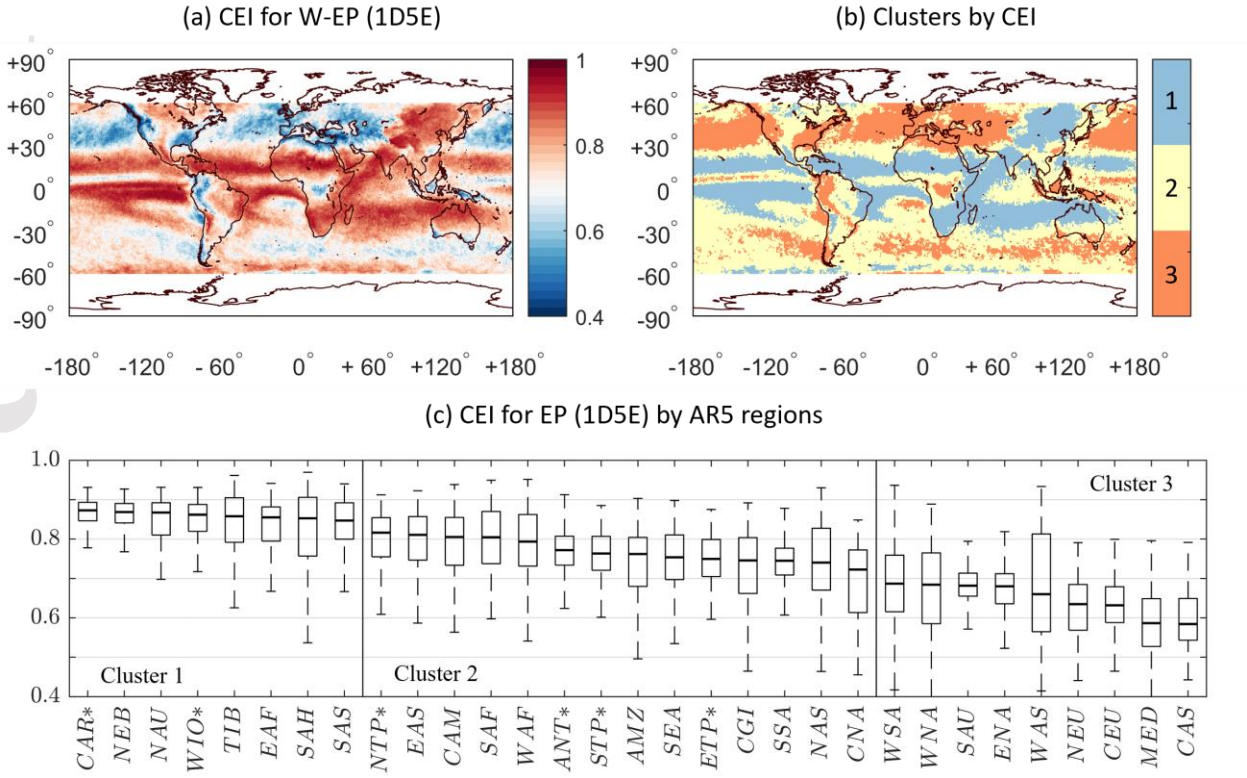

Figure 4. Results of Concurrent Extremes Index (CEI) analysis, presenting (a) spatial distributions of CEI for EP (1D5E), (b) three global clusters presenting the W-EP relevance segmented by CEI magnitudes, and (c) CEI for 1D5E in descending order for IPCC's AR5 regions. Note ALA (Alaska/N.W. Canada) and ARC* (Arctic) are not included.

Figure 4 presents the results of the global CEI analysis. As shown in Figure 4a, the strength of the W-EP relationship as represented by CEI is strongest across the tropical regions (within ±30°). However, exceptions are observed over mountainous and basin landforms including the northern Andes in South America, the Congo Basin in central Africa, and the Southeast Asian Archipelago. These areas in the tropics match the tropical rainforest climate type (Beck et al., 2018), with high mean annual precipitation and high mean apportionment entropy (AE) (Konapala et al., 2020)—the higher the AE value is, the less variable the monthly precipitation or evaporation is. The strength of the W-EP relationship is noticeably reduced in regions outside ±30°, including

most of Europe and central Asia in the northern hemisphere and the southern tip of South Africa, southern Australia, and New Zealand in the southern hemisphere. Here, the inland regions of North America and East Asia are exceptions. The regional differences in the strength of the W-EP relationship as indicated by the CEI values is visualised through the adaptive K-means clustering algorithm (Dixit, 2021) and presented in Figure 4b. This clustering helps to identify areas where EP is more (or less) related to extreme W, with stronger W-EP associations being found in Cluster 1 and weaker associations in Clusters 2 and 3. Aggregating the regional results in Figure 4a and 4b by the AR5 regions, the distributions of CEI are presented as the boxplot in Figure 4c. Counting the most frequent cluster numbers in each region, a total of 8 regions from CAR (small islands regions Caribbean) to SAS (South Asia) belong to Cluster 1 (i.e., high W-EP relevance), and the remaining 23 regions from NTP (Pacific Islands region) to CAS (Central Asia) are included in Clusters 2 or 3 (i.e., low W-EP relevance). Among the 8 regions included in Cluster 1, as shown in Figure 1c, upward trends of W are observed in five of these regions with CAR (small islands regions Caribbean), NAU (North Australia), and TIB (Tibetan Plateau) being exceptions. In particular, the three regions of WIO (West Indian Ocean), SAS (South Asia), and EAF (East Africa) have considerably increasing W and high CEIs, and in general, EPs are expected to greatly increase with increasing W in these regions, as compared to the other regions. Also, when we perform a CEI analysis considering only rainy days, the spatial pattern of CEI is similar to Figure 4a. While the overall CEI value is 0 to 0.1 lower than when all data are used, the key conclusions of this study about the regional differences and patterns of CEI remain unchanged.

Based on this framework, we next conduct a sensitivity analysis of the W-EP relationship for various durations of precipitation accumulation (D) and the average number of events per year (N). The baseline is the 1D5E that we have used previously, and the three different conditions for the sensitivity analysis are 5D5E, 1D10E, and 5D10E (i.e., five largest 5-day events per year on average, and the ten largest 1-day and 5-day events). CEI maps for the three conditions and boxplots for comparison are presented in Figure 5 below.

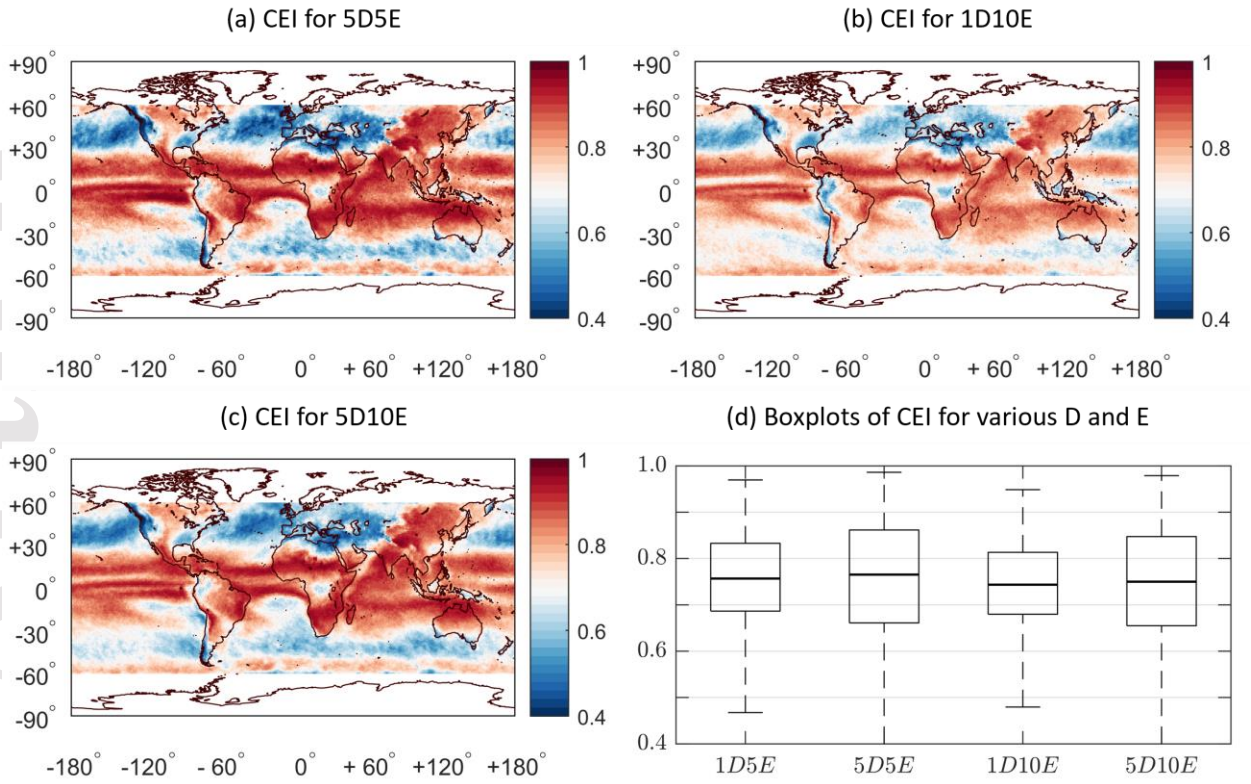

Figure 5. Results of sensitivity analysis for CEI with various days of precipitation cumulation (D) and the average number of events per year (N). CEI maps of (a) 5D5E, (b) 1D10E, and (c) 5D10E. (d) presents boxplots for comparing the baseline (1D5E) and the three conditions.

Examining Figure 5a and d, the 5D5E spatial pattern and distribution of CEI are similar to those of 1D5E. However, for this longer duration, there is a greater divergence (spread) in the CEI values, that is, regions that had a low CEI for 1D5E are now smaller, and regions that a high CEI are now greater. For 1D10E, the tropical (within ±30°) and non-tropical (above ±30°) regions differ less (Figure 5b), albeit with a similar spatial pattern to 1D5E and 5D5E. As shown in Figure 5d, while the 2nd and 3rd quartiles of CEI for 1D10E are lower, the 1st quartile is similar or a bit lower than those of 1D5E and 5D5E. That is, the EP for 1D10E becomes less relevant to W (low CEI), and the regional differences in the W-EP relationship over the tropical and non-tropical regions is less (narrower interquartile range). In Figure 5c, the spatial pattern of 5D10E is similar to that of 1D10E, but it is observed that the regional differences in the W-EP relationship over the tropical and non-tropical regions are more contrasting (wider interquartile range). Furthermore, the interquartile range of 5D10E is lowest among the four cases as presented in Figure 5d. These results suggest that EP is more strongly associated with W (i.e., higher CEI for EPs) in the tropics, and the regional differences in the W-EP relationship are more contrasting (i.e., wide interquartile range) as D increases, with the strength of the W-EP relationship weaker (lower CEI) as E increases.

5. Discussion and Implications

The atmospheric mass balance (1) is the result of complex dynamic and thermodynamic interactions of atmospheric components (Seager et al., 2010; Su & Smith, 2021). Based on the various datasets considered, this study investigated how W and P, two elements of the atmospheric

mass balance, are connected and how they change with rising temperatures. In addition, based on this relationship, we investigated evidence for informing the projection of EP to future temperature increase. To this end, we found positive correlations between W and SAT (DPT) and increasing trends of W in many regions of the world, suggesting that W is likely to increase under further increases to temperature with climate change. We also found that the strength of the W-EP relationship (as represented by the CEI for EPs) is strongest in the tropics, where the greatest uncertainty exists in EP projection. This suggests the W-EP relationship could potentially be used to improve EP projections. The regional differences in the W-EP relationship mean that the direct contribution of W to EP differs with climate, suggesting that in the regions where the W-EP relationship is weak (i.e., low CEI), it may be necessary to consider the interrelationships with other components such as wind and evaporation to develop a stronger W-EP relationship. Based on the results presented here, there are several natural extensions to this work.

The CEI-based W-EP relation could be used to derive simple EP projections, especially in regions where these are overwhelmingly high. A conditional relationship between the two variables, as suggested in (Roderick et al., 2020), can be formulated. This can be used in conjunction with projections of W with temperature or time, obtainable from the relationship with temperature (SAT or DTP) (Figure 2) or directly projected from GCMs. This, or analogous methods, could aid EP projection in high CEI regions, particularly where GCM uncertainty of EP projections is the greatest. In this case, instead of estimating EP from W using a simple linear relationship, it would be better to estimate EP from the CEI once the CDFs of W and P have been obtained from the GCM outputs.

The work could also be extended to different time scales. For example, it has been shown that intermittence of P can affect the relationship between P and SAT (and hence W and SAT) (Schleiss, 2018; Visser et al., 2020). Repeating the work here using sub-daily data may allow the findings here to be further generalized to finer time scales and to regions that do not exhibit strong relations at the daily timescales considered here. The relatively short record length here, though possibly influenced by decadal variability, has been assumed to be indicative of climate change. Using data for 20–30 years or longer may provide deeper insights. For example, W trends in the early 21st century may be greater than those of the late 20th century due to the intensification of the global warming effect in recent years. For this, however, satellite (observational) data will be insufficient and reanalysis products will need to be considered. However, by using this longer data, it may be possible to test how consistent the EP projections made using the CEI-based method are with historical data.

The proposed CEI-based projection approach can be also used for investigating the frequency of EPs with relation to W. That is, it may be possible to interpret and project the EP in terms of return period by examining how many EPs above a certain threshold occur each year (or during a specific period) conditional on the concurrent value of W. This is especially pertinent as both reanalysis and GCM datasets exhibit greater consistency (reduced uncertainty) for variables such as SAT, DTP or W when compared to the EPs which exhibit greater instability (Eghdamirad et al., 2017; Kim et al., 2020).

Finally, while the strong W-EP relevance of tropical and East Asian regions represented by high CEI values raises some insights and possible applications, it is necessary to further investigate why high-latitude regions exhibit relatively low CEI values. Considering the association of EP with various factors, such as water vapor transport, which were not considered in this study, will aid the understanding of EP mechanisms globally.

6. Conclusions

In this study, we investigated the relationship between daily extreme precipitation (EP) and corresponding total precipitable water (W) at a global scale by analysing 17-years of data from 2003 to 2019. For this, we used the GPM IMERG final product for P and focused on the satellite-derived AIRS product for W. To confirm consistency of the results, we also used four W products from reanalyses, including MERRA2, ERA5, JRA-55, and NCEP. Together with this, we examined the relationship between the variables (P and W) and temperatures by using the 2-m surface air temperature (SAT) and the 2-m dew point temperature (DPT) from ERA5-Land. This study identified the following key findings which answer the three primary questions raised in the introduction.

1. *How is W impacted by climate change?*

   All monthly W data have averages around 24 mm/month and consistently exhibit statistically significant upward trends during the 17-year study period. The upward trends are predominant worldwide, with the strongest trends being present in tropical land regions within ±30°. The Pearson correlation (R) between daily W and DPT is strongly positive across the globe. However, weakly positive to moderately negative R between daily W and SAT is observed over the tropical rainforests. This negative correlation can be explained by the limitations of temperature due to evaporation in hot climates (Roderick et al., 2019), and/or the cooling effect due to local evapotranspiration over tropical rainforests (Ellison et al., 2017; Lejeune et al., 2015; Y. Li et al., 2015). One can thus conclude that W can be expected to increase into the future, with increases most notable over tropical land regions.

2. *Does EP correspond to coincident W extremes, and whether this correspondence is homogenous in space?*

   We quantified the strength of the W-EP relationship using the Concurrent Extremes Index (CEI)—the higher the CEI, the stronger being the W-EP relationship. For EPs defined as the five largest 1-day events per year on average (1D5E), high CEI values were found across the tropical regions (within ±30°) with exceptions over the tropical rainforest climate. The relevance of W-EP is noticeably reduced in regions outside ±30° except for the inland regions of North America and East Asia. We identified five AR5 regions where both increasing W and high CEIs are observed, indicative of EPs that are likely to increase under climate change. These are NEB (North-East Brazil), WIO (West Indian Ocean), EAF (East Africa), SAH (Sahara), and SAS (South Asia). In particular, both the tendencies of increasing W and high CEIs are notable in WIO, SAS, and EAF compared to other regions, suggesting daily duration EP increases are expected to be most pronounced in these parts of the world.

3. *Does this correspondence hold across different durations and thresholds of EP?*

   From a sensitivity analysis of the W-EP relationship across multiple days of precipitation accumulation (D) and the average number of events per year (E), EP is consistently identified as more relevant to W in the tropics; the regional differences in the W-EP relationship between the tropics and non-tropics become greater as D increases; and EP tends to be less relevant to W as E increases.

Acknowledgments

This research was supported by the Australian Research Council (ARC) Discovery project DP200101326 and by industry support from Hydro Tasmania, Melbourne Water, Murray- Darling Basin Authority, Queensland Department of Natural Resources Mines and Energy, Seqwater, Snowy Hydro, Sunwater, Water Corporation WA, and WaterNSW.

Data Availability Statement

All data used for this study are freely available. GPM IMERG final, AIRS, MERRA2 products are available from https://earthdata.nasa.gov/; ERA5 from https://cds.climate.copernicus.eu/cdsapp#!/home; JRA-55 and NCEP from https://rda.ucar.edu/.

References

AIRS project. (2019). *Aqua/AIRS L3 Daily Standard Physical Retrieval (AIRS-only) 1 degree × 1 degree V7.0*.

Alexander, L. V., Zhang, X., Peterson, T. C., Caesar, J., Gleason, B., Klein Tank, A., et al. (2006). Global observed changes in daily climate extremes of temperature and precipitation. *Journal of Geophysical Research: Atmospheres*, *111*(D5).

Ali, H., Fowler, H. J., & Mishra, V. (2018). Global observational evidence of strong linkage between dew point temperature and precipitation extremes. *Geophysical Research Letters*, *45*(22), 12,320–312,330.

Ali, H., & Mishra, V. (2017). Contrasting response of rainfall extremes to increase in surface air and dewpoint temperatures at urban locations in India. *Scientific Reports*, *7*(1), 1228.

Anabalón, A., & Sharma, A. (2017). On the divergence of potential and actual evapotranspiration trends: An assessment across alternate global datasets. *Earth's Future*, *5*(9), 905–917.

Bao, J., Sherwood, S. C., Alexander, L. V., & Evans, J. P. (2017). Future increases in extreme precipitation exceed observed scaling rates. *Nature climate change*, *7*(2), 128.

Barbero, R., Westra, S., Lenderink, G., & Fowler, H. J. (2018). Temperature- extreme precipitation scaling: a two- way causality? *International Journal of Climatology*, *38*, e1274–e1279.

BBC (Producer). (2021, 3 Aug 2021). Europe floods: Victims face massive clean-up as waters recede. Retrieved from https://www.bbc.com/news/world-europe-57876982

Beck, H. E., Pan, M., Roy, T., Weedon, G. P., Pappenberger, F., Van Dijk, A. I. J. M., et al. (2019). Daily evaluation of 26 precipitation datasets using Stage-IV gauge-radar data for the CONUS. *Hydrology and Earth System Sciences*, *23*(1), 207-224.

Beck, H. E., Zimmermann, N. E., McVicar, T. R., Vergopolan, N., Berg, A., & Wood, E. F. (2018). Present and future Köppen-Geiger climate classification maps at 1-km resolution. *Scientific Data, 5*, 180214.

Bock, O., Keil, C., Richard, E., Flamant, C., & Bouin, M. n. (2005). Validation of precipitable water from ECMWF model analyses with GPS and radiosonde data during the MAP SOP. *Quarterly Journal of the Royal Meteorological Society: A journal of the atmospheric sciences, applied meteorology and physical oceanography, 131*(612), 3013–3036.

Chester, M. V., Underwood, B. S., & Samaras, C. (2020). Keeping infrastructure reliable under climate uncertainty. *Nature climate change, 10*(6), 488–490.

Cornwall, W. (2021). Europe's deadly floods leave scientists stunned. *Science, 373*(6553), 372–373.

Dixit, A. (2021). Adaptive kmeans Clustering for Color and Gray Image. (https://www.mathworks.com/matlabcentral/fileexchange/45057-adaptive-kmeans-clustering-for-color-and-gray-image), MATLAB Central File Exchange. Retrieved July 6, 2021.

Donat, M. G., Alexander, L. V., Yang, H., Durre, I., Vose, R., Dunn, R. J. H., et al. (2013). Updated analyses of temperature and precipitation extreme indices since the beginning of the twentieth century: The HadEX2 dataset. *Journal of Geophysical Research: Atmospheres, 118*(5), 2098–2118.

Donat, M. G., Lowry, A. L., Alexander, L. V., O'Gorman, P. A., & Maher, N. (2016). More extreme precipitation in the world's dry and wet regions. *Nature climate change, 6*(5), 508–513.

Eghdamirad, S., Johnson, F., & Sharma, A. (2017). How reliable are GCM simulations for different atmospheric variables? *Climatic Change, 145*, 237–248.

Ellison, D., Morris, C. E., Locatelli, B., Sheil, D., Cohen, J., Murdiyarso, D., et al. (2017). Trees, forests and water: Cool insights for a hot world. *Global Environmental Change, 43*, 51–61.

Encyclopedia Britannica. (2020). Rainforest. In The Editors of Encyclopaedia (Ed.).

Fujita, M., & Sato, T. (2017). Observed behaviours of precipitable water vapour and precipitation intensity in response to upper air profiles estimated from surface air temperature. *Scientific Reports, 7*(1), 1–6.

Garcia, D. (2010). Robust smoothing of gridded data in one and higher dimensions with missing values. *Computational Statistics & Data Analysis, 54*(4), 1167–1178.

Gelaro, R., McCarty, W., Suárez, M. J., Todling, R., Molod, A., Takacs, L., et al. (2017). The modern-era retrospective analysis for research and applications, version 2 (MERRA-2). *Journal of Climate*, *30*(14), 5419–5454.

Guo, Y., Wu, Y., Wen, B., Huang, W., Ju, K., Gao, Y., & Li, S. (2020). Floods in China, COVID-19, and climate change. *The Lancet Planetary Health*, *4*(10), e443–e444.

Helsel, D. R., & Hirsch, R. M. (1992). *Statistical methods in water resources* (Vol. 49): Elsevier.

Hersbach, H., Bell, B., Berrisford, P., Hirahara, S., Horanyi, A., Munoz-Sabater, J., et al. (2020). The ERA5 global reanalysis. *Quarterly Journal of the Royal Meteorological Society*, *146*(730), 1999–2049.

Hirsch, R. M., Slack, J. R., & Smith, R. A. (1982). Techniques of trend analysis for monthly water quality data. *Water Resources Research*, *18*(1), 107–121.

Ho, S.-P., Peng, L., Mears, C., & Anthes, R. A. (2018). Comparison of global observations and trends of total precipitable water derived from microwave radiometers and COSMIC radio occultation from 2006 to 2013. *Atmospheric Chemistry and Physics*, *18*(1), 259–274.

Huffman, G. J., Bolvin, D. T., Braithwaite, D., Hsu, K., Joyce, R., Xie, P., & Yoo, S.-H. (2015). NASA global precipitation measurement (GPM) integrated multi-satellite retrievals for GPM (IMERG). *Algorithm Theoretical Basis Document (ATBD) Version*, *4*, 26.

IPCC. (2021). Climate Change 2021: The Physical Science Basis. Contribution of Working Group I to the Sixth Assessment Report of the Intergovernmental Panel on Climate Change [Masson-Delmotte, V., P. Zhai, A. Pirani, S. L. Connors, C. Péan, S. Berger, N. Caud, Y. Chen, L. Goldfarb, M. I. Gomis, M. Huang, K. Leitzell, E. Lonnoy, J. B. R. Matthews, T. K. Maycock, T. Waterfield, O. Yelekçi, R. Yu and B. Zhou (eds.)]. Cambridge University Press. In Press.

Jiang, J., Zhou, T., & Zhang, W. (2019). Evaluation of satellite and reanalysis precipitable water vapor data sets against radiosonde observations in central Asia. *Earth and Space Science*, *6*(7), 1129–1148.

Johnson, F., & Sharma, A. (2009). Measurement of GCM Skill in Predicting Variables Relevant for Hydroclimatological Assessments. *Journal of Climate*, *22*(16), 4373–4382.

Kendall, M. G. (1948). *Rank correlation methods*. Oxford, England: Griffin.

Kharin, V. V., Zwiers, F. W., Zhang, X., & Wehner, M. (2013). Changes in temperature and precipitation extremes in the CMIP5 ensemble. *Climatic Change*, *119*(2), 345–357.

Kim, S., Anabalón, A., & Sharma, A. (2021). An Assessment of Concurrency in Evapotranspiration Trends across Multiple Global Datasets. *Journal of Hydrometeorology*, *22*(1), 231–244.

Kim, S., Eghdamirad, S., Sharma, A., & Kim, J. H. (2020). Quantification of Uncertainty in Projections of Extreme Daily Precipitation. *Earth and Space Science, 7*(8), e2019EA001052.

Kobayashi, S., Ota, Y., Harada, Y., Ebita, A., Moriya, M., Onoda, H., et al. (2015). The JRA-55 reanalysis: General specifications and basic characteristics. *Journal of the Meteorological Society of Japan, 93*(1), 5–48.

Konapala, G., Mishra, A. K., Wada, Y., & Mann, M. E. J. N. C. (2020). Climate change will affect global water availability through compounding changes in seasonal precipitation and evaporation. *Nature communications, 11*(1), 1–10.

Kunkel, K. E., Karl, T. R., Easterling, D. R., Redmond, K., Young, J., Yin, X., & Hennon, P. (2013). Probable maximum precipitation and climate change. *Geophysical Research Letters, 40*(7), 1402–1408.

Kunkel, K. E., Karl, T. R., Squires, M. F., Yin, X., Stegall, S. T., & Easterling, D. R. (2020). Precipitation extremes: Trends and relationships with average precipitation and precipitable water in the contiguous United States. *Journal of Applied Meteorology and Climatology, 59*(1), 125–142.

Kunkel, K. E., Stevens, S. E., Stevens, L. E., & Karl, T. R. (2020). Observed climatological relationships of extreme daily precipitation events with precipitable water and vertical velocity in the contiguous United States. *Geophysical Research Letters, 47*(12), e2019GL086721.

Lejeune, Q., Davin, E. L., Guillod, B. P., & Seneviratne, S. I. (2015). Influence of Amazonian deforestation on the future evolution of regional surface fluxes, circulation, surface temperature and precipitation. *Climate Dynamics, 44*(9), 2769–2786.

Lenderink, G., & Attema, J. (2015). A simple scaling approach to produce climate scenarios of local precipitation extremes for the Netherlands. *Environmental Research Letters, 10*(8), 085001.

Lenderink, G., Mok, H. Y., Lee, T. C., & Van Oldenborgh, G. J. (2011). Scaling and trends of hourly precipitation extremes in two different climate zones–Hong Kong and the Netherlands. *Hydrology and Earth System Sciences, 15*(9), 3033–3041.

Li, X., & Long, D. (2020). An improvement in accuracy and spatiotemporal continuity of the MODIS precipitable water vapor product based on a data fusion approach. *Remote Sensing of Environment, 248*, 111966.

Li, Y., Zhao, M., Motesharrei, S., Mu, Q., Kalnay, E., & Li, S. (2015). Local cooling and warming effects of forests based on satellite observations. *Nature communications, 6*(1), 1–8.

Mann, H. B. (1945). Nonparametric Tests Against Trend. *Econometrica, 13*(3), 245–259.

Manola, I., Hurk, B. v. d., Moel, H. D., & Aerts, J. C. J. H. (2018). Future extreme precipitation intensities based on a historic event. *Hydrology and Earth System Sciences, 22*(7), 3777–3788.

Mears, C. A., Santer, B. D., Wentz, F. J., Taylor, K. E., & Wehner, M. F. (2007). Relationship between temperature and precipitable water changes over tropical oceans. *Geophysical Research Letters, 34*(24).

Mears, C. A., Smith, D. K., Ricciardulli, L., Wang, J., Huelsing, H., & Wentz, F. J. (2018). Construction and uncertainty estimation of a satellite- derived total precipitable water data record over the world's oceans. *Earth and Space Science, 5*(5), 197–210.

Nayak, S., & Takemi, T. (2019). Dependence of extreme precipitable water events on temperature. *Atmósfera, 32*(2), 159–165.

O'Gorman, P. A., & Schneider, T. (2009). The physical basis for increases in precipitation extremes in simulations of 21st-century climate change. *Proceedings of the National Academy of Sciences, 106*(35), 14773–14777.

O, S., Foelsche, U., Kirchengast, G., Fuchsberger, J., Tan, J., & Petersen, W. A. (2017). Evaluation of GPM IMERG Early, Late, and Final rainfall estimates using WegenerNet gauge data in southeastern Austria. *Hydrol. Earth Syst. Sci., 21*(12), 6559-6572. https://hess.copernicus.org/articles/21/6559/2017/

O'Gorman, P. A. (2012). Sensitivity of tropical precipitation extremes to climate change. *Nature Geoscience, 5*(10), 697–700.

O'Gorman, P. A., & Muller, C. J. (2010). How closely do changes in surface and column water vapor follow Clausius–Clapeyron scaling in climate change simulations? *Environmental Research Letters, 5*(2), 025207.

Pfahl, S., O'Gorman, P. A., & Fischer, E. M. (2017). Understanding the regional pattern of projected future changes in extreme precipitation. *Nature climate change, 7*(6), 423.

Pham, H. T., Kim, S., Marshall, L., & Johnson, F. (2019). Using 3D robust smoothing to fill land surface temperature gaps at the continental scale. *International Journal of Applied Earth Observation and Geoinformation, 82*, 101879.

Prein, A. F., Rasmussen, R. M., Ikeda, K., Liu, C., Clark, M. P., & Holland, G. J. (2017). The future intensification of hourly precipitation extremes. *Nature climate change, 7*(1), 48.

Roderick, T. P., Wasko, C., & Sharma, A. (2019). Atmospheric moisture measurements explain increases in tropical rainfall extremes. *Geophysical Research Letters, 46*(3), 1375–1382.

Roderick, T. P., Wasko, C., & Sharma, A. (2020). An improved covariate for projecting future rainfall extremes? *Water Resources Research, 56*(8), e2019WR026924.

Roman, J., Knuteson, R., Ackerman, S., & Revercomb, H. (2015). Predicted changes in the frequency of extreme precipitable water vapor events. *Journal of Climate, 28*(18), 7057–7070.

Saha, S., Moorthi, S., Pan, H.-L., Wu, X., Wang, J., Nadiga, S., et al. (2010). The NCEP climate forecast system reanalysis. *Bulletin of the American Meteorological Society, 91*(8), 1015–1058.

Saha, S., Moorthi, S., Wu, X., Wang, J., Nadiga, S., Tripp, P., et al. (2014). The NCEP climate forecast system version 2. *Journal of Climate, 27*(6), 2185–2208.

Schleiss, M. (2018). How intermittency affects the rate at which rainfall extremes respond to changes in temperature. *Earth System Dynamics, 9*(3), 955–968.

Seager, R., Naik, N., & Vecchi, G. A. (2010). Thermodynamic and dynamic mechanisms for large-scale changes in the hydrological cycle in response to global warming. *Journal of Climate, 23*(17), 4651–4668.

Sen, P. K. (1968). Estimates of the Regression Coefficient Based on Kendall's Tau. *Journal of the American Statistical Association, 63*(324), 1379–1389.

Seneviratne, S., Nicholls, N., Easterling, D., Goodess, C., Kanae, S., Kossin, J., et al. (2012). Changes in climate extremes and their impacts on the natural physical environment. In: Managing the Risks of Extreme Events and Disasters to Advance Climate Change Adaptation. A Special Report of Working Groups I and II of the Intergovernmental Panel on Climate Change (IPCC) [C. B. Field, V. Barros, T. F. Stocker, D. Qin, D. J. Dokken, K. L. Ebi, M. D. Mastrandrea, K. J. Mach, G. -K. Plattner, S. K. Allen, M. Tignor and P. M. Midgley (eds.)]. Cambridge University Press, Cambridge, United Kingdom, and New York, NY, USA, pp. 109-230.

Sharma, A., Hettiarachchi, S., & Wasko, C. (2021). Estimating design hydrologic extremes in a warming climate: alternatives, uncertainties and the way forward. *Philosophical Transactions of the Royal Society A, 379*(2195), 20190623.

Shi, F., Xin, J., Yang, L., Cong, Z., Liu, R., Ma, Y., et al. (2018). The first validation of the precipitable water vapor of multisensor satellites over the typical regions in China. *Remote Sensing of Environment, 206*, 107–122.

Sih, A., Ferrari, M. C. O., & Harris, D. J. (2011). Evolution and behavioural responses to human- induced rapid environmental change. *Evolutionary applications, 4*(2), 367–387.

Sillmann, J., Kharin, V. V., Zwiers, F. W., Zhang, X., & Bronaugh, D. (2013). Climate extremes indices in the CMIP5 multimodel ensemble: Part 2. Future climate projections. *Journal of Geophysical Research: Atmospheres, 118*(6), 2473–2493.

Su, Y., & Smith, J. A. (2021). An Atmospheric Water Balance Perspective on Extreme Rainfall Potential for the Contiguous US. *Water Resources Research, 57*(4), e2020WR028387.

Sun, Q., Zhang, X., Zwiers, F., Westra, S., & Alexander, L. V. (2021). A global, continental, and regional analysis of changes in extreme precipitation. *Journal of Climate, 34*(1), 243–258.

Syvitski, J. P. M., & Brakenridge, G. R. (2013). Causation and avoidance of catastrophic flooding along the Indus River, Pakistan. *GSA Today, 23*(1), 4–10.

Theil, H. (1992). A Rank-Invariant Method of Linear and Polynomial Regression Analysis. In B. Raj & J. Koerts (Eds.), *Henri Theil's Contributions to Economics and Econometrics: Econometric Theory and Methodology* (pp. 345–381). Dordrecht: Springer Netherlands.

Utsumi, N., Seto, S., Kanae, S., Maeda, E. E., & Oki, T. (2011). Does higher surface temperature intensify extreme precipitation? *Geophysical Research Letters, 38*(16).

Visser, J. B., Wasko, C., Sharma, A., & Nathan, R. (2020). Resolving inconsistencies in extreme precipitation- temperature sensitivities. *Geophysical Research Letters, 47*(18), e2020GL089723.

Wang, G., Garcia, D., Liu, Y., De Jeu, R., & Dolman, A. J. (2012). A three-dimensional gap filling method for large geophysical datasets: Application to global satellite soil moisture observations. *Environmental Modelling & Software, 30*, 139–142.

Wang, Y., Yang, K., Pan, Z., Qin, J., Chen, D., Lin, C., et al. (2017). Evaluation of precipitable water vapor from four satellite products and four reanalysis datasets against GPS measurements on the Southern Tibetan Plateau. *Journal of Climate, 30*(15), 5699–5713.

Wasko, C., Lu, W. T., & Mehrotra, R. (2018). Relationship of extreme precipitation, dry-bulb temperature, and dew point temperature across Australia. *Environmental Research Letters, 13*(7), 074031.

Wasko, C., Parinussa, R. M., & Sharma, A. (2016). A quasi-global assessment of changes in remotely sensed rainfall extremes with temperature. *Geophysical Research Letters, 43*(24), 12,659–612,668.

Wasko, C., Westra, S., Nathan, R., Orr, H. G., Villarini, G., Villalobos Herrera, R., & Fowler, H. J. (2021). Incorporating climate change in flood estimation guidance. *Philosophical Transactions of the Royal Society A, 379*(2195), 20190548.

Westra, S., Fowler, H. J., Evans, J. P., Alexander, L. V., Berg, P., Johnson, F., et al. (2014). Future changes to the intensity and frequency of short-duration extreme rainfall. *Reviews of Geophysics, 52*(3), 522–555.

WMO. (2009). *Manual on estimation of probable maximum precipitation (PMP)*: World meteorological organization.

Worawiwat, A., Chaleeraktrakoon, C., & Sharma, A. (2021). Is increased flooding in Bangkok a result of rising local temperatures? *Journal of Hydrology X*, 100095.

World Bank. (2012). *Thai flood 2011: Rapid assessment for resilient recovery and reconstruction planning*. Retrieved from https://openknowledge.worldbank.org/handle/10986/26862

Wright, D. B., Bosma, C. D., & Lopez- Cantu, T. (2019). US hydrologic design standards insufficient due to large increases in frequency of rainfall extremes. *Geophysical Research Letters, 46*(14), 8144–8153.

Yu, L., Leng, G., Python, A., & Peng, J. (2021). A Comprehensive Evaluation of Latest GPM IMERG V06 Early, Late and Final Precipitation Products across China. *Remote Sensing, 13*(6), 1208.

Zhang, D., Huang, J., Guan, X., Chen, B., & Zhang, L. (2013). Long-term trends of precipitable water and precipitation over the Tibetan Plateau derived from satellite and surface measurements. *Journal of Quantitative Spectroscopy and Radiative Transfer*, *122*, 64–71.

Zhang, W., Villarini, G., & Wehner, M. (2019). Contrasting the responses of extreme precipitation to changes in surface air and dew point temperatures. *Climatic Change, 154*(1-2), 257–271.